nature communications

Article

https://doi.org/10.1038/s41467-024-55521-2

Engineering 2D spin networks by on-surface encapsulation of azafullerene radicals in nanotemplates

Received: 20 August 2024

Accepted: 14 December 2024

Published online: 02 January 2025

Check for updates

Gregor Kladnik[1,2,11], Luca Schio[2,11], Gregor Bavdek[2,3,11], Yuri Tanuma[4], Marion van Midden Mavrič[4], Erik Zupanič[4], Bastien Anézo[4,5], Ioanna K. Sideri[6], Nikos Tagmatarchis[6], Jannis Volkmann[7,8], Hermann A. Wegner[7,8], Andrea Goldoni[9], Christopher P. Ewels[5], Alberto Morgante[2,10], Luca Floreano[2], Denis Arčon[1,4] ✉ & Dean Cvetko[1,2,4] ✉

We present an efficient strategy for on-surface engineering of organic metal-free supramolecular complexes with long-term spin protection. By vacuum deposition of azafullerene ($C_{59}N^{\bullet}$) monomers on a pre-deposited template layer of [10]cycloparaphenylene ([10]CPP) nanohoops on Au(111) surface we exploit the molecular shape matching between the $C_{59}N^{\bullet}$ and [10]CPP for the azafullerene encapsulation with nanohoops in a guest-host complexation geometry. $C_{59}N^{\bullet}\subset$[10]CPP supramolecular complexes self-assemble into an extended two-dimensional hexagonal lattice yielding a high density network of stable spin-1/2 radicals. We find compelling evidence for electronic coupling between the guest $C_{59}N^{\bullet}$ and the host [10]CPP in supramolecular species. At the same time, [10]CPP effectively protects the radical state of encapsulated azafullerenes against dimerization and inhibits $C_{59}N^{\bullet}$ coupling to the Au substrate. Azafullerene encapsulation by nanohoops represents a viable realization of molecular spin protection while simultaneously demonstrating exceptional self-assembling properties by which large-scale 2D architectures of molecular spins can be realized.

Stable molecular spins are considered as the simplest platform to encode molecular qubits. In this context, considerable progress has been achieved employing molecules with a transition metal as a spin-active center[1,2]. The alternative, metal-free organic molecular systems, show a natural tendency to self-assemble and in principle provide an excellent playground for designing large-scale architectures of molecular spins. Moreover, weak spin-orbit coupling in purely organic radicals enables very long spin-coherence times required for manipulation of spin states[3–7]. However, owing to their high reactivity the long-term stability of molecular transition-metal-free organic radicals remains a major challenge in stabilization[8,9], detection and manipulation[10] that has yet to be satisfactorily solved, especially for extended radical arrays. This is particularly important as any complex architecture of molecular spins must ultimately be placed in some two-

[1]Faculty of Mathematics and Physics, University of Ljubljana, Ljubljana, Slovenia. [2]CNR-IOM, Istituto Officina dei Materiali, Basovizza Area Science Park, Trieste, Italy. [3]Faculty of Education, University of Ljubljana, Ljubljana, Slovenia. [4]Jožef Stefan Institute, Ljubljana, Slovenia. [5]Institut des Matériaux de Nantes Jean Rouxel (IMN), UMR 6502 CNRS, Nantes University, Nantes, France. [6]Theoretical and Physical Chemistry Institute, National Hellenic Research Foundation, Athens, Greece. [7]Institute of Organic Chemistry, Justus Liebig University Giessen, Giessen, Germany. [8]Center for Materials research (ZfM/LaMa), Justus Liebig University Giessen, Giessen, Germany. [9]Elettra Sincrotrone Trieste S.C.p.A., Basovizza, Trieste, Italy. [10]Physics department, University of Trieste, Trieste, Italy. [11]These authors contributed equally: Gregor Kladnik, Luca Schio, Gregor Bavdek. ✉e-mail: denis.arcon@ijs.si; dean.cvetko@fmf.uni-lj.si

dimensional (2D) network on solid substrate[6]. The stability of such molecular spins then decisively relies on sufficiently weak interaction of organic radicals with the substrate and suppressed intermolecular coupling into non-radical assemblies.

One promising spin-active candidate for the robust organic molecular spins is azafullerene radical, $C_{59}N^{\bullet}$, where one nitrogen replaces a carbon atom on the fullerene skeleton. Due to valence inequality between N and C, $C_{59}N^{\bullet}$ is a closed-cage hetero-fullerene radical where the odd electron resides on a carbon atom neighboring the embedded nitrogen[11,12]. The $C_{59}N^{\bullet}$ monomers are highly reactive radicals which rapidly form diamagnetic dimers $(C_{59}N)_2$ both, in powder and in multilayer films[12–14]. The spin-active species can be accessed by thermolysis or photolysis of the parent $(C_{59}N)_2$[7,15–18], but they are nevertheless still highly reactive to re-dimerization and/or oxidation (in ambient environment). On crystalline substrates, like Au(111), $C_{59}N^{\bullet}$ can be ultra-high vacuum (UHV) deposited in the form of radical monomers, yet due to interaction with the Au the radical state in the $C_{59}N^{\bullet}$ monolayer is partially quenched[19]. With thermal annealing the intermolecular coupling into nonmagnetic dimers prevails[14]. Interestingly, $C_{59}N^{\bullet}$ monomers in the non-contact second layer deposited on top of the first passivating monolayer retain their radical state thanks to the reduced interaction with the Au(111) substrate[19].

Recently, we proposed an alternative more robust strategy for long-term stabilization of azafullerene radicals by encapsulating them with protective molecular nanobelts in the form of [10]cycloparaphenylene ([10]CPP) nanohoops[7,18,20]. This guest-host assembly approach exploits the supramolecular shape matching based on concave–convex π–π interaction between the nanobelt-[10]CPP and $C_{59}N^{\bullet}$, enabling the formation of $C_{59}N^{\bullet}\subset$[10]CPP radical complexes in solution or in powder. The electron paramagnetic resonance signal observed after high-temperature treatment comprises characteristic ^{14}N hyperfine splitting of $C_{59}N^{\bullet}\subset$[10]CPP and was traced even after several months, which is in striking contrast to pristine $(C_{59}N)_2$[7]. Such stable $C_{59}N^{\bullet}\subset$[10]CPP spin-1/2 entities in powder also show remarkably long spin coherence times. Hence, the $C_{59}N^{\bullet}$ radicals protected by the [10]CPP nanohoops fulfill many of the major criteria for the realization of molecular spin qubits and could, together with the design flexibility offered by CPPs, provide an excellent platform for the bottom-up approach to quantum circuits of qubits.

Synthesis of encapsulated azafullerenes on solid substrates on the other hand, and their manipulation into 2D network architectures have not been reported so far and a direct observation of single encapsulated complexes as well as their spectroscopic characterization are still lacking. Herein we report on experimental and theoretical study of engineering large scale 2D layers of encapsulated azafullerenes on gold. The synthesis of supramolecular $C_{59}N^{\bullet}\subset$[10]CPP assemblies on Au(111) is performed by $C_{59}N^{\bullet}$ monomer deposition on a pre-deposited template monolayer of hexagonally packed [10]CPP rings adsorbed flat on the Au(111). The accommodation of $C_{59}N^{\bullet}$ proceeds in a shape-matched guest-host assembly with $C_{59}N^{\bullet}$ trapped at the hollow centers of the flat lying [10]CPP molecules thus promoting the [10]CPP encapsulation of azafullerenes. High-resolution X-ray spectroscopy and Scanning-Tunnelling-Microscopy (STM) topographic imaging provide firm evidence of electronic coupling in $C_{59}N^{\bullet}$-[10]CPP complexes, and demonstrate the crucial role of [10]CPP for $C_{59}N^{\bullet}$ radical stability and protection against coupling into non-magnetic dimers, thereby unlocking the potential of organic radicals for quantum technologies.

Results

Structure and morphology of on-surface synthesized $C_{59}N^{\bullet}\subset$[10]CPP assemblies

In Fig. 1a we present step-by-step analysis of $C_{59}N^{\bullet}\subset$[10]CPP on-surface encapsulation and supramolecular ordering in 2D networks by carbon and nitrogen X-ray photoemission spectroscopy (XPS) for (i) [10]CPP monolayer template on Au(111) followed by (ii) the deposition of 11 Å thick layer of $C_{59}N^{\bullet}$ on-top of the pre-formed [10]CPP monolayer at room temperature (RT) and, (iii–v) subsequent annealing effects on XPS spectra of the heterolayer. XPS for the reverse deposition sequence of [10]CPP grown on the layer of $C_{59}N$/Au(111) is shown in Fig. 1b (vi–viii).

Whereas the C1*s* XPS peak of the [10]CPP multilayer is found at 284.4 eV binding energy (BE, Fig. S1), the C1*s* peak of the [10]CPP monolayer on Au(111) (Fig.1a curve i) shifts to 283.5 eV (gray color) due to [10]CPP interaction with Au(111) (see Supporting info for [10]CPP-Au coupling details) and core-hole screening by the metallic substrate. For the as-deposited 11 Å thick layer of $C_{59}N$ on-top of the [10]CPP/Au (ii) we observe dominant C1*s* and N1*s* peaks at 284.9 eV and 400.6 eV, respectively, reminiscent of the $C_{59}N$ multilayer (red color)[19]. In fact, 11 Å thick layer of $C_{59}N$ corresponds to 1.5 ML of densely packed $C_{59}N$ molecules on Au(111) (ref. 19) or equivalently to >3 ML of $C_{59}N$ when referred to the molecular density of the [10]CPP/Au template layer (Fig. S2). However, we observe also additional C1*s* and N1*s* XPS peaks at 284.3 eV and 400.0 eV, respectively (blue color), neither found for the $C_{59}N$ multilayer nor for the pristine $C_{59}N$ monolayer in contact with Au(111) (at 284.6 eV and 400.3 eV, respectively)[19]. These additional peaks of the heterolayer are indicative of new electronic state due to $C_{59}N^{\bullet}$-[10]CPP coupling (*vide infra*). The C1*s* and N1*s* peaks of the coupled $C_{59}N^{\bullet}$/[10]CPP assemblies (blue color) grow in intensity with the post-deposition annealing (iii–v) and dominate the XPS spectra after annealing to 300–340 °C, indicating that supramolecular assemblies become the majority phase upon the annealing treatment.

In Fig. 1d we show STM topographic image of [10]CPP monolayer on Au(111) at RT with highly ordered, flat lying nanohoops assembled in hexagonally packed 2D islands with molecular rows principally oriented at ≈10° from the [1–10] surface direction of the Au(111). We note that ordered [10]CPP islands cover large areas, indicating high mobility and long-range diffusion of [10]CPP molecules over the Au(111) surface already at RT. [10]CPP molecules within the 2D islands can be identified as circular rings with a hollow structure in the middle. The dimension of these nanohoops within the islands is estimated from the STM height profile across the nanohoops as 14.4 ± 0.7 Å in diameter (peak-to-peak) with nearest-neighbor center-to-center distance of 16.9 ± 0.5 Å. These dimensions match well with the geometrical diameter of the [10]CPP molecule (≈14 Å) in a flat-lying adsorption geometry[21] and resemble the DFT calculated sheet of [10]CPP with center-to-center distance of ~16.8 Å (Fig. S9). The circular ring-like shapes observed in the STM topographs also indicate the absence of any significant structural deformation similar to [12]CPP molecules weakly coupled with isotropic surfaces such as Cu(100)[22]. When $C_{59}N^{\bullet}$ molecules are deposited on-top of the [10]CPP monolayer, they appear as bright round objects positioned preferentially in the central hollow regions of the [10]CPP rings (Fig. 1e). $C_{59}N^{\bullet}$ molecules thus spontaneously form an adsorbate phase commensurate with the [10]CPP layer beneath. Upon temperature annealing we observe further ordering of the $C_{59}N^{\bullet}$/[10]CPP heterolayer into ever larger hexagonally packed islands of $C_{59}N^{\bullet}\subset$[10]CPP supramolecular complexes commensurate with the layer of bare [10]CPP (Fig. 1f, g).

The process of supramolecular encapsulation on Au(111) is followed by the STM height profile analysis. For the as-deposited $C_{59}N^{\bullet}$ at RT the STM apparent height profile taken across the [10]CPP island with the $C_{59}N^{\bullet}$ adsorbed on-top yields the [10]CPP-to-$C_{59}N^{\bullet}$ apparent height difference (peak-to-peak) of 3.8 Å (Fig. 2a). We also note that a small fraction of $C_{59}N^{\bullet}$ sits at somewhat lower heights, indicating that when the $C_{59}N^{\bullet}\subset$[10]CPP complex sits on Au the equatorial planes of the [10]CPP and that of $C_{59}N^{\bullet}$ do not coincide. The variation in apparent height suggests that for $C_{59}N^{\bullet}\subset$[10]CPP on Au the complexation may yield an outward displacement of the $C_{59}N$ center with respect to that of [10]CPP. Our DFT calculations of $C_{59}N^{\bullet}\subset$[10]CPP complexation on Au(111) confirm that stable complexes on Au(111)

https://doi.org/10.1038/s41467-024-55521-2

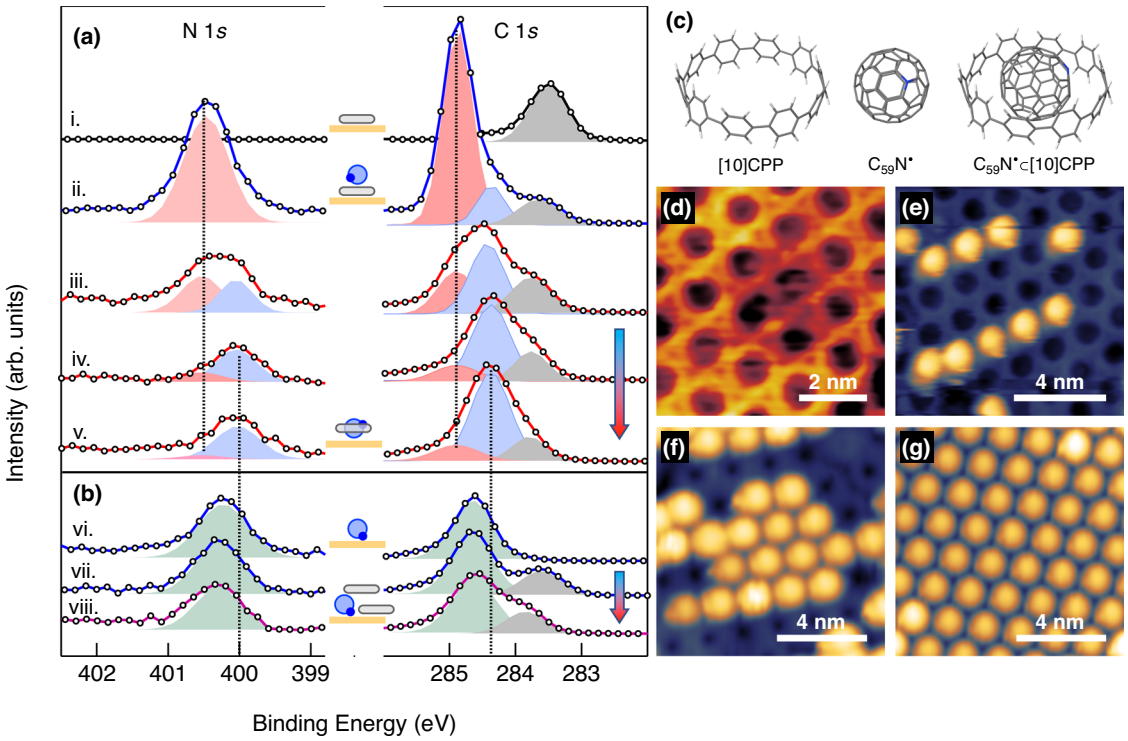

Fig. 1 | $C_{59}N^{\bullet}$⊂[10]CPP on-surface encapsulation and supramolecular ordering in 2D. a Nitrogen and carbon 1*s* XPS of [10]CPP/Au(111) (i), and of as-deposited $C_{59}N^{\bullet}$ on top of [10]CPP layer on Au (ii), followed by thermal annealing to (iii) 300 °C (1 min), (iv) 340 °C (4 min), and (v) 340 °C (10 min). Spectral decomposition shows azafullerene components of the thick layer (red), encapsulated $C_{59}N^{\bullet}$⊂[10]CPP (blue), and [10]CPP (gray). **b** N1*s* and C1*s* XPS of $C_{59}N$ monolayer on Au(111) (vi) and of as-deposited [10]CPP on $C_{59}N$/Au (vii) followed by thermal annealing to 300 °C (viii). Spectral decomposition shows C1*s* and N1*s* peaks of the $C_{59}N$/Au layer (green) and for the [10]CPP (gray). Dotted vertical lines at energies 400.6 eV (284.9 eV) and 400 eV (284.3 eV) indicate the binding energy of $C_{59}N$ nitrogen (carbon) core levels in the multilayer and monolayer on Au(111), respectively. The measured binding energies are consistent with those reported in ref. 19. In the cartoons $C_{59}N$ (blue circles with a dot), [10]CPP rings (gray ellipses) and Au(111) surface (dark yellow thick line) are schematically presented. The two thick arrows indicate the direction of increasing temperature upon annealing. Lines between data points serve as a guide to the eye. **c** Stick representation of [10]CPP and $C_{59}N^{\bullet}$ molecules and of the $C_{59}N^{\bullet}$⊂[10]CPP complex. STM topographic images of [10]CPP/Au(111) layer **d** and $C_{59}N^{\bullet}$ deposition on [10]CPP/Au at RT (**e**) followed by thermal annealing to 220 °C (**f**) and 320 °C (**g**). Large areas of hexagonally packed $C_{59}N^{\bullet}$⊂[10]CPP islands are observed after annealing to 320 °C (**g**). Each annealing step was performed by sample transfer into the preparation chamber (no vacuum breaking), then the sample was brought back into the STM scanning stage. Therefore, images shown in (**e**–**g**) do not show the same microlocation. The apparent height is represented by a false color map (black-blue-yellow).

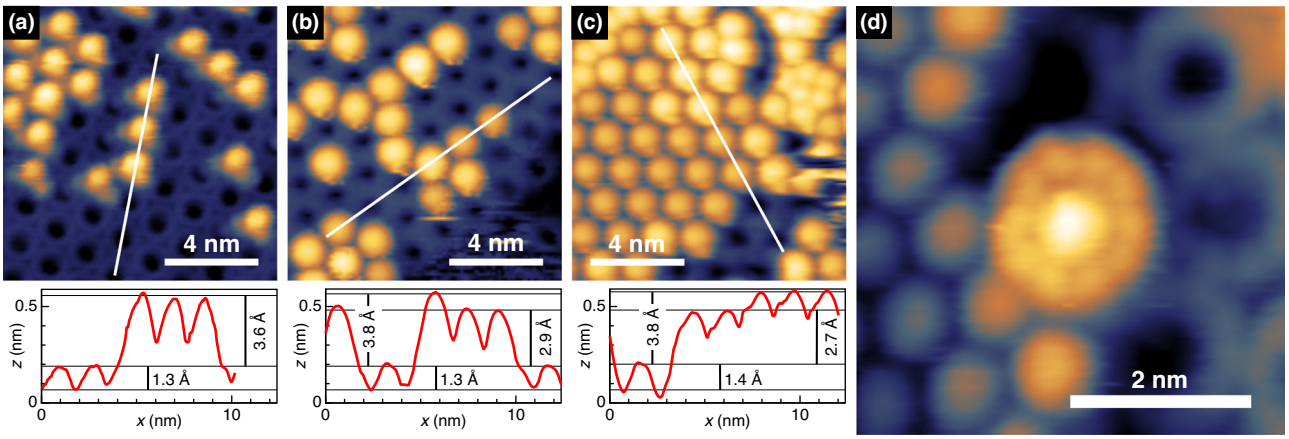

Fig. 2 | The fine structure of $C_{59}N^{\bullet}$⊂[10]CPP supramolecular complex. a STM image of $C_{59}N$/[10]CPP/Au(111) layer deposited at RT (top) shown with apparent height profile (bottom) along the depicted white line; **b** STM image and height profile for the same sample, annealed to 220 °C and **c** annealed further to 320 °C. **d** High resolution topographic image of the $C_{59}N^{\bullet}$⊂[10]CPP supramolecular assembly captured at a terrace edge between $C_{59}N$/Au island and [10]CPP/Au island. The apparent height is represented by a false color map (black-blue-yellow).

indeed display guest-host configurations with the guest $C_{59}N$ center of mass residing slightly above the center of mass of the host [10]CPP (Fig. S11). In addition, the calculated energy gains due to $C_{59}N^{\bullet}$⊂[10]CPP complexation are larger than 2.3 eV, which makes these supramolecular structures remarkably resilient against any high-temperature treatment.

Interestingly, upon thermal annealing, the vertical offset between the $C_{59}N^{\bullet}$ and [10]CPP centers in the complex is on average reduced, as

https://doi.org/10.1038/s41467-024-55521-2

witnessed by the STM apparent height profile shown in Fig. 2b, c, where the [10]CPP-to-$C_{59}N^{\bullet}$ apparent height difference for the 220 °C (320 °C) annealed heterolayers measures a substantially lower value of 2.9 Å. The observed change indicates some degree of structural relaxation of $C_{59}N^{\bullet}$ within the complex on Au(111) taking place with annealing. Such 2D layer of relaxed $C_{59}N^{\bullet}\subset$[10]CPP complexes can be readily recognized from the STM images in Fig. 2b, c as layer of objects with slightly lower brightness which eventually prevail in the topographic image of the film annealed at 320 °C (Fig. 1g). We note that with annealing the $C_{59}N^{\bullet}$ accommodates within the [10]CPP template layer to optimize the geometry of $C_{59}N^{\bullet}\subset$[10]CPP radical complex. Thereby, the apparent height of $C_{59}N^{\bullet}$ relative to the Au(111) substrate is reduced. At the same time, we note that C1*s* NEXAFS peak assigned to [10]CPP changes after annealing thus demonstrating that encapsulation affects the [10]CPP phenyls too. This experimental observation is in excellent agreement with our DFT calculations in which the [10]CPP nanoring relaxes its phenyl ring dihedral angles during the encapsulation process. Specifically, the original phenyl dihedral angle for the [10]CPP molecule adsorbed on Au(111) is 20.6°. When $C_{59}N^{\bullet}$ is trapped inside the [10]CPP as shown in Fig. S11b, the final dihedral angles of the phenyl groups in the $C_{59}N^{\bullet}\subset$[10]CPP radical complex vary from 22.9° to 27.4°.

A high resolution STM topographic image of a single supramolecular $C_{59}N^{\bullet}\subset$[10]CPP unit (Fig. 2d) displays an example of nanohoop encapsulation that has been captured at the border between adjacent islands of $C_{59}N$/Au(111) and [10]CPP/Au(111). Such anchoring suppresses some of the fast $C_{59}N^{\bullet}$ and/or [10]CPP dynamics otherwise inherent to molecular structures adsorbed on Au(111) surface. This dynamics suppression enables a dramatical improvement in spatial resolution of observed STM image where, e.g., individual phenyl rings can now be clearly observed as a 10-fold azimuthal modulation in intensity reflecting the exemplary $C_{59}N^{\bullet}\subset$[10]CPP supramolecular structure. This unit measures ≈17 Å in diameter in line with the geometrical structure of the $C_{59}N^{\bullet}\subset$[10]CPP supramolecular assembly.

The important role of [10]CPP as a template layer on Au(111) with its guest-host adsorption geometry promoting the on-surface encapsulation synthesis is further revealed in a reverse co-deposition scheme where a layer of closely packed $C_{59}N$/Au(111) is formed first and [10]CPP molecules are adsorbed on-top afterwards. Figure 1b shows XPS spectra of the bare $C_{59}N$ layer on Au(111), (vi) of as-deposited [10]CPP on-top (vii) and of the heterolayer after annealing (viii). The C1*s* (N1*s*) peak here shows a major component at 284.6 eV (400.3 eV) binding energy characteristic of the $C_{59}N$ monolayer in contact with Au(111)[19], whereas new core level components associated with the encapsulated $C_{59}N^{\bullet}\subset$[10]CPP assemblies hardly develop. In support of the XPS data, STM images of the [10]CPP grown on-top of pre-deposited $C_{59}N$/Au(111) show the preference for growth of separate islands of $C_{59}N$/Au and [10]CPP/Au (Fig. S7).

Guest-host coupling in hooped $C_{59}N^{\bullet}\subset$[10]CPP assemblies

The electronic coupling between the frontier orbitals of [10]CPP and $C_{59}N^{\bullet}$ at the interface between [10]CPP and $C_{59}N^{\bullet}$ molecular layers is studied step-by-step throughout the process of azafullerene encapsulation by NEXAFS and resonant photoemission spectroscopy (RPES). We note that in such supramolecular structure (Fig. 2d), the [10]CPP acts as size and shape matched host to the azafullerene guest in the center. The phenyl rings of the CPP host embrace the azafullerene cage at ~3.4–3.7 Å separation (see Fig. S13), resulting in large contact area between the guest-host molecules with their π orbitals extended in the space between[23]. The supramolecular encapsulation is expected to affect [10]CPP π orbital coupling and delocalization which can be directly measured by NEXAFS and RPES, respectively. In Fig. 3 we show Carbon K-edge NEXAFS measured for pristine $C_{59}N$ and [10]CPP films as well as for the $C_{59}N$/[10]CPP heterolayer throughout the synthesis of supramolecular $C_{59}N^{\bullet}\subset$[10]CPP complexes. For the pristine [10]CPP

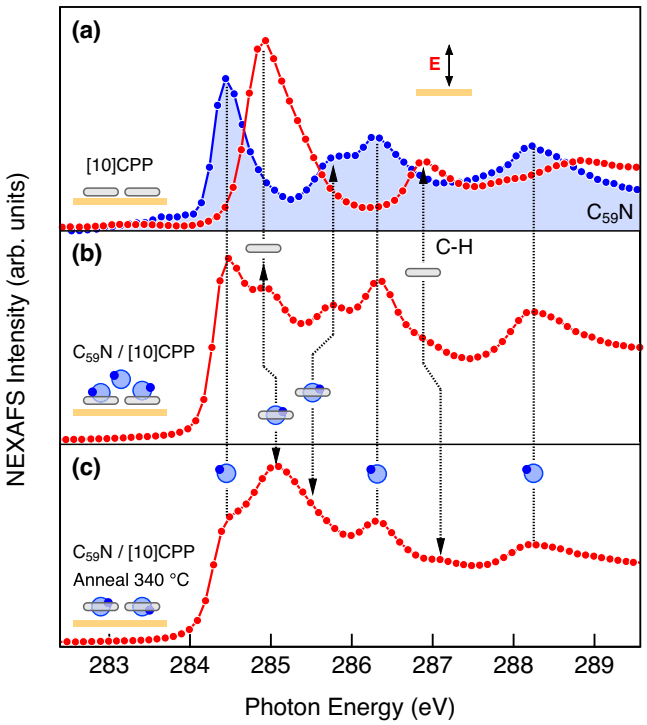

Fig. 3 | The electronic coupling between the molecular orbitals of host [10]CPP and guest $C_{59}N^{\bullet}$. Carbon K-edge NEXAFS: **a** of [10]CPP/Au(111) layer (red curve) and $C_{59}N$/Au(111) layer (blue filled curve), **b** of $C_{59}N$/[10]CPP heterolayer on Au(111) at RT and **c** of $C_{59}N^{\bullet}\subset$[10]CPP supra-molecular complex layer on Au(111) after annealing to 340 °C. All spectra were taken with photon polarization in transverse magnetic geometry (*p*-polarization), i.e., electric field vector perpendicular to the Au substrate surface (see cartoon on top). Vertical dashed lines serve as guides to the eye indicating the energy shifts of $C_{59}N$ (in cartoons depicted as blue circles with a dot) and [10]CPP (gray ellipses) supramolecular orbital levels from those of respective pristine layers with post-deposition annealing.

layer on Au(111) we observe the main peak at 285 eV photon energy that corresponds to the resonant excitation from C1*s*→$LUMO_{CPP}$ with π symmetry (red curve), similar to biphenyl molecules following the building block approach[24,25]. We note, that the $LUMO_{CPP}$ is polarized normally to the CPP phenyl rings and is therefore naturally involved in the orbital coupling with azafullerene when the latter is encapsulated by [10]CPP.

NEXAFS spectroscopic features for the $C_{59}N$ layer deposited at RT on the pre-deposited [10]CPP template layer may be recognized at distinct photon energies $h\nu$ = 284.4 eV, 285.8 eV and 286.3 eV (blue shaded curve, Fig. 3) and correspond to the known electronic excitations from C1*s* to $LUMO_{aza}$, $LUMO_{aza}$+1 and $LUMO_{aza}$+2 orbitals of the $C_{59}N$, respectively (see Fig. S12 for DFT calculation)[26,27]. Upon thermal annealing the C1*s* NEXAFS of the heterorganic layer displays spectroscopic changes that are attributed to the electronic coupling associated with the formation of $C_{59}N^{\bullet}\subset$[10]CPP complexes. In particular, $LUMO_{CPP}$ of the of $C_{59}N^{\bullet}\subset$[10]CPP shifts to higher energies by 0.15 eV, whereas $LUMO_{aza}$+1 shifts to lower energies by 0.2 eV (Fig. 3). The observed shift of the $LUMO_{aza}$+1 in the supramolecular complex resembles the reported shift of empty orbitals on the $Y_2@C_{79}N$ when hooped with [12]CPP leading to reduced HOMO-LUMO gap in the respective supramolecular complex[28]. We note however, that part of the observed shift for the [10]CPP unoccupied levels may also result from the modified coupling of [10]CPP template layer with Au(111) surface, occurring in the process of $C_{59}N^{\bullet}\subset$[10]CPP encapsulation.

Intermolecular electronic coupling at the $C_{59}N$-[10]CPP interface is further addressed by X-ray RPES. Fullerenes are well known for their electron affinity as their t_{1u} unoccupied orbitals are easily accessible for

https://doi.org/10.1038/s41467-024-55521-2

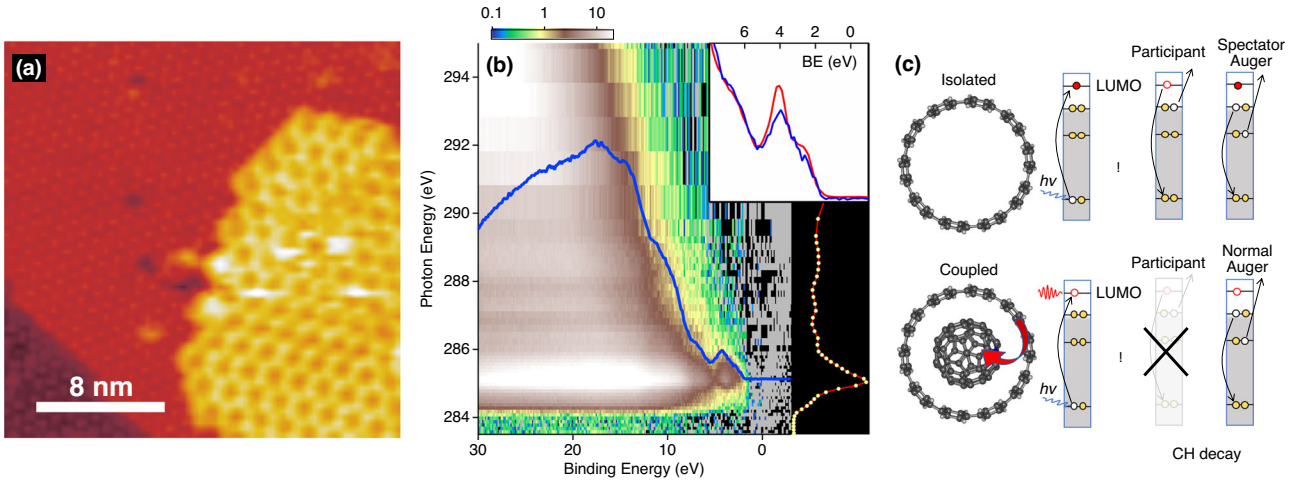

Fig. 4 | The charge transfer dynamics between the coupled [10]CPP and $C_{59}N$ molecules. Reverse-order deposition of [10]CPP/$C_{59}N$/Au heterolayer. **a** STM topographic image of [10]CPP island on-top of $C_{59}N$ layer displaying CPP-$C_{59}N$ interface isolated from the Au(111). The apparent height is represented by a false color map (black-red-yellow). **b** Carbon K-edge RPES map of [10]CPP adlayer on $C_{59}N$/Au is shown in a 2D color map of intensity versus photon energy (vertical axis) and electron binding energy (BE, horizontal axis). The NEXAFS signal across the same photon energy range is shown aside on the top axis (yellow markers). Intensity quenching of the participant signal (blue curve) relative to its benchmark signal from the [10]CPP multilayer (red curve, for full RPES map see Fig. S4a) is detailed in the inset. **c** Schematic energy level diagram of the core hole (CH) decay following the core→lowest unoccupied molecular orbital (LUMO) excitation is shown for isolated (upper) and coupled (bottom) [10]CPP. Ultrafast delocalization of the core excited electron in the $LUMO_{CPP}$ is depicted as charge transfer from the [10]CPP→$C_{59}N$, leading to the observed quenching of the participant Auger decay channel. Dark yellow filled circles represent electrons, empty (white) circles represent holes. The core-excited electron is shown as a red filled circle. Different possible electron transitions are indicated with arrows.

charge transfer (CT)[29]. Therefore, when an electron is excited to the unfilled orbital of the [10]CPP ($LUMO_{CPP}$) the electronic orbital coupling between the [10]CPP and $C_{59}N$ molecules is manifested as ultrarapid charge delocalization from the original $LUMO_{CPP}$ orbital. Such charge delocalization can be measured at the interface between the pristine layers of coupled $C_{59}N$ and [10]CPP species within the core-hole-clock (CHC) implementation of the RPES experiments[30]. However, we cannot directly access the CT dynamics from the $LUMO_{CPP}$ of the [10]CPP to the $C_{59}N$ in the $C_{59}N^{\bullet}$⊂[10]CPP layer on Au(111) as these supramolecular complexes are also in direct contact with the Au substrate where CT to the metallic substrate dominates. In fact, for the [10]CPP monolayer on Au, the [10]CPP molecules couple to the Au(111) and ultrafast delocalization from the $LUMO_{CPP}$ to the Au empty band is measured with CT time $\tau_{CT} < 6$fs (Fig. S4). Equally fast CT time is measured for the $C_{59}N$/[10]CPP/Au(111) layer where azafullerenes are adsorbed on-top of the [10]CPP monolayer on Au(111) because ultrafast CT from the [10]CPP to Au prevails the LUMO delocalization dynamics even when $C_{59}N$ is adsorbed on-top.

To single out $LUMO_{CPP}$ delocalization dynamics to the $C_{59}N$ we thus need to isolate the [10]CPP-$C_{59}N$ interface from the Au(111) surface, so we focus on RPES measurements for the [10]CPP layer adsorbed on-top of pre-deposited $C_{59}N$/Au(111) (Fig. 4). STM topographic image (Fig. 4a) and the control XPS measurement of C1*s* XPS for the [10]CPP adlayer (Fig. S3, $E_{C1s} = 284.4$ eV), both confirm that for thus prepared sample the deposited [10]CPP molecules adsorb on the $C_{59}N$ layer and are not in direct contact with the Au(111). Fig. 4b shows RPES intensity across the C K-edge as a 2D color map versus the photon energy (left axis) and binding energy (bottom axis). Single photoemission spectrum collected from this 2D RPES map at the C1*s*→$LUMO_{CPP}$ excitation (red curve overlaid at hν ≈ 284 eV) shows a broad Auger peak and several resonantly enhanced peaks in the upper valence band due to *participant Auger* decay of the core-hole[30]. The occurrence of these *participant* resonances in the RPES spectrum reflects the participation of the C1*s*→$LUMO_{CPP}$ excited electron in the core-hole-decay via Auger electron emission. However, upon ultrarapid delocalization of the core-excited electrons from the $LUMO_{CPP}$ the intensity of participant resonances is quenched (Fig. S5). By quantifying the participant intensity quenching we estimate the degree of orbital delocalization in the coupled system in terms of CT time (τ_{CT})[30,31]. In the inset of Fig. 4a we show the resonant photoemission spectrum (I_p) over restricted energy range together with the benchmark spectrum from its' uncoupled counterpart system in the [10]CPP multilayer (I_{pO}). The relative quenching of the participant resonances in the [10]CPP/$C_{59}N$/Au system is then estimated to be $\beta = I_p/I_{pO} \geq 0.76$ yielding the $LUMO_{CPP}$→$C_{59}N$ CT time $\tau_{CT} = \tau_{ch}\ \beta/(1-\beta) \leq 19 \pm 1$ fs, where carbon core-hole lifetime $\tau_{ch} \approx 6$ fs is used[32]. The upper bound used for the CT time estimation has a twofold reason; first we assume that electronic coupling of the [10]CPP multilayer resembles that of an isolated system, yet multilayer molecules may already be partly coupled to each other when compared to true gas phase system. This then upscales the estimated participant intensity of the isolated system (I_{pO}). And secondly, not all [10]CPP molecules of the heterolayer may be effectively coupled to the $C_{59}N$ guests leading to, on average, lower quenching of the measured system (I_p). The obtained CT time relates to the strength of orbital interaction in the coupled system and may be compared to similar coupled organic systems. For example, ultrashort τ_{CT} have been measured for chemically bonded atomic sulfur on ruthenium (<0.3 fs)[33], amine lone-pair binding to Au (<1 fs)[34], intermolecular amino-carboxyl coupling (~10 fs)[35] and also between π−π stacked aromatic systems like paracyclophanes; [2,2]-PCP (~3 fs) and [4,4]-PCP (~50 fs)[36]. Taking the geometrical distance between the guest-host aromatic systems in $C_{59}N^{\bullet}$⊂[10]CPP of ~3.4–3.7 Å deduced from our DFT calculations (see Fig. S13), the obtained τ_{CT} relates well with those for the [2,2]-PCP and [4,4]-PCP with ~3 Å and 4 Å separation between aromatic rings, respectively[36]. Similar ultrafast CT dynamics (~16 fs) has been observed also between shape-matched donor-acceptor molecules in related guest-host pairs of hexabenzocoronenes (HBC) and C_{60}[37]. Finally, strong interaction between [10]CPP and fullerenes in similar guest-host supramolecular assemblies has been found also for $Li^{+}@C_{60}$⊂[10]CPP where significant delocalization of the positive charge to the whole complex has been reported[38].

https://doi.org/10.1038/s41467-024-55521-2

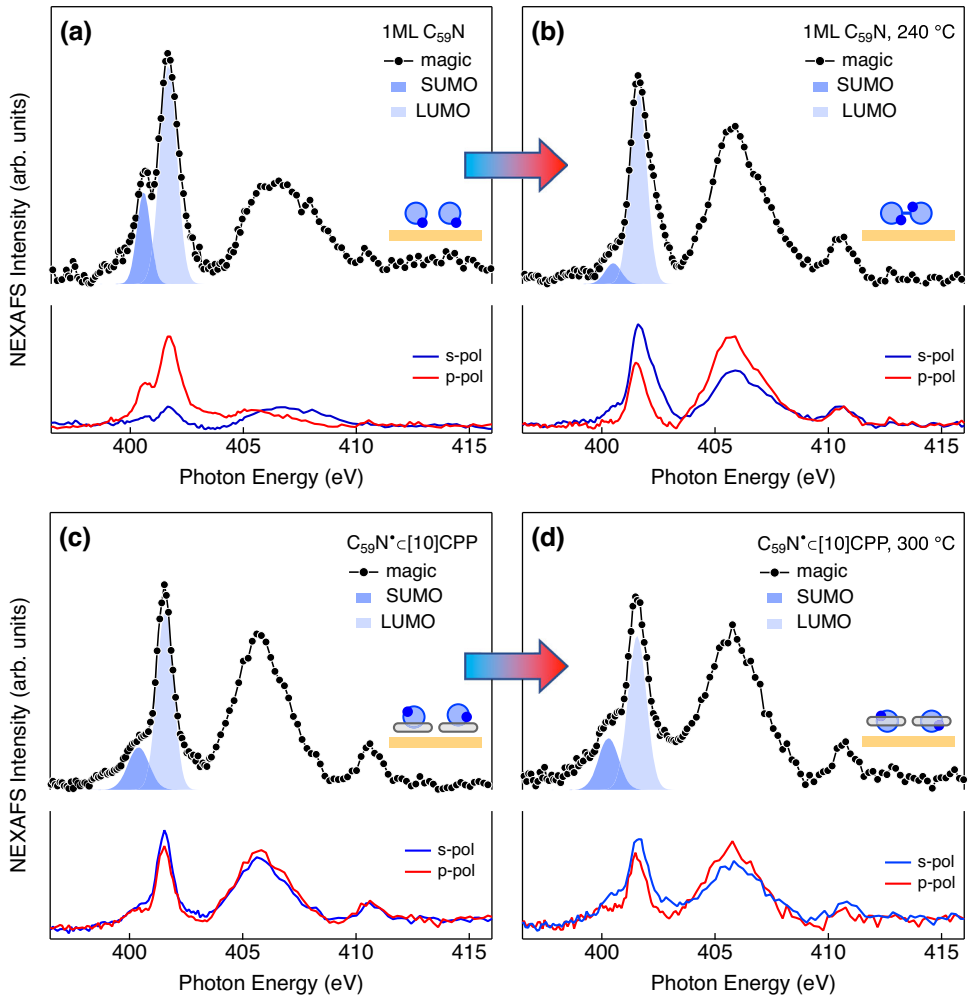

Fig. 5 | Radical protection and stability of $C_{59}N^{\bullet}\subset$[10]CPP assemblies. a Nitrogen K-edge NEXAFS of a layer of $C_{59}N$ monomers on Au at RT, and **b** after annealing to 240 °C whereupon a layer of $(C_{59}N)_2$ dimers is formed. **c** Nitrogen K-edge NEXAFS of encapsulated $C_{59}N^{\bullet}\subset$[10]CPP layer at RT, and **d** after annealing to 300 °C. Black lines with markers are spectra represented in "magic angle" polarization geometry, and red/blue curves are spectra taken with photon in transverse magnetic/transverse electric polarization (p-pol/s-pol), respectively. The spectral fits of the singly unoccupied molecular orbital (SUMO, dark blue) and lowest unoccupied molecular orbital (LUMO, light blue) peaks are also shown. Thick arrows indicate the annealing step. In the cartoons $C_{59}N$ (blue circles with a dot), [10]CPP rings (gray ellipses) and Au(111) surface (dark yellow thick line) are schematically presented.

Radical protection and stability of $C_{59}N^{\bullet}\subset$[10]CPP assemblies

We have recently identified the spectroscopic fingerprint of the $C_{59}N$ radical state from the N K-edge NEXAFS resonances as the excitation from N1*s* core level to the singly unoccupied molecular orbital (SUMO) peak at 400.7 eV which is observed for early deposition stages of azafullerene on Au(111)[19]. Its relative peak intensity reaches almost 35% that of the LUMO main line (401.3 eV) for 1^+ ML films, whereas it is less than 11% for the mostly non-radical multilayer of $(C_{59}N)_2$ dimers[14,19]. Moreover, the $C_{59}N$ layer of monomers on Au(111) is unstable against annealing to 240 °C whereupon it dimerizes and the radical state of $C_{59}N^{\bullet}$ monomers is lost.

This temperature instability is presented in Fig. 5 where N K-edge NEXAFS is shown for the layer of $C_{59}N$ monomers on Au(111) at RT (a) and after annealing to 240 °C (b) whereupon a layer of dimers $(C_{59}N)_2$ forms. The relative SUMO intensity reminiscent of the radical state decreases by a factor of ~3 upon annealing, as evidenced by the peak fits (dark blue color). At the same time, we observe a significant change in the linear dichroism of the LUMO signal in the N K-edge NEXAFS indicating an average reorientation of the $C_{59}N$ molecules[19,25]. In fact, the azafullerene cages are found to orient with their N sites predominantly along the surface plane after annealing, consistently with their in-plane coupling into non-magnetic $(C_{59}N)_2$ dimers. The radical stability against dimerization, however, is drastically improved for the layer of encapsulated supramolecular assemblies of $C_{59}N^{\bullet}\subset$[10]CPP. In the N K-edge NEXAFS spectra for the $C_{59}N^{\bullet}\subset$[10]CPP layer taken before and after temperature annealing to 340 °C (Fig. 5c, d) respectively, the relative SUMO peak intensity (28–33% of the LUMO) proves that by encapsulation the radical state of the $C_{59}N^{\bullet}$ monomers is preserved and remains stable even upon annealing to 340 °C. At the same time, N K-edge NEXAFS spectra lack any linear dichroism indicating that there is almost no preferred orientation of the azafullerene cage when protected by the [10]CPP, which is entirely consistent with the N-based orbitals and the radical state of azafullerene being isolated and well protected by the [10]CPP ring.

Electronic coupling of the N-based orbitals in the unprotected $(C_{59}N)_2$ and encapsulated $C_{59}N^{\bullet}\subset$[10]CPP layers is further assessed from Nitrogen K-edge RPES (Fig. S6). Direct comparison of Resonant Auger peak at the N1*s*→LUMO resonance shows a significant blueshift of the *spectator Auger* (~2 eV in kinetic energy, KE) for the $C_{59}N^{\bullet}\subset$[10]CPP assembly but not for $(C_{59}N)_2$/Au. This shift is reminiscent of negligible delocalization of the core excited electrons from the N-based unoccupied orbitals and confirms that N-based LUMO in the encapsulated radical assembly is effectively isolated and protected from coupling with the Au(111). The protective shielding by the nanohoop

evidently extends also on the neighboring carbon in the azafullerene cage, where the singly occupied orbital of the $C_{59}N^{\bullet}$ radical is mainly located. The [10]CPP encapsulation therefore provides valuable protection of the $C_{59}N$ radical against interaction and dimerization, which stabilizes the azafullerene's spin state on a long timescale.

In conclusion, we have demonstrated a viable route for on-surface engineering of large-scale supramolecular $C_{59}N^{\bullet}\subset$[10]CPP networks with hexagonal packing by vacuum deposition of $C_{59}N^{\bullet}$ monomers on-top of a pre-deposited monolayer of [10]CPP on Au(111). The flat lying [10]CPP monolayer serves as a template layer that favors adsorption of $C_{59}N^{\bullet}$ in the central hollow region of the [10]CPP molecules in a guest-host coupling scheme whereupon the interaction between the $C_{59}N^{\bullet}$ and the [10]CPP template is optimized. The process of supramolecular encapsulation is manifested in the occurrence of new core level states in the XPS spectra of N1*s* and C1*s*, and in hybridization of the carbon based $C_{59}N^{\bullet}$ and [10]CPP unfilled orbitals when $C_{59}N^{\bullet}\subset$[10]CPP assemblies are formed.

Importantly, unlike for pristine $C_{59}N$ the radical state of encapsulated $C_{59}N^{\bullet}\subset$[10]CPP is greatly stabilized, as no dimerization nor coupling with the substrate is found even after annealing to 340°C, hence yielding extended 2D networks of spin-1/2 protected supramolecular units with hexagonal packing. The robustness of encapsulated $C_{59}N^{\bullet}\subset$[10]CPP able to self-organize into 2D lattices of spin-1/2 protected organic radicals may open intriguing opportunities in manipulating lattices of weakly coupled molecular spins for 2D circuits of qubits and/or for the surface chemistry with organic radicals.

Methods

$(C_{59}N)_2$ and [10]CPP synthesis and characterization

Azafullerene dimer $(C_{59}N)_2$ was synthesized following the standard procedure described in literature and following our recent synthetic protocol[12,19]. High-performance liquid chromatography (HPLC) was performed for the further purification of the $(C_{59}N)_2$. The purification method for the parent $(C_{59}N)_2$ component involves (a) column chromatography in o-DCB, (b) recrystallization in o-DCB/MeOH, and (c) preparative HPLC (toluene as mobile phase, concentration of 1 mg/mL and flow rate of 8 mL/min)—see Fig. S8a for a schematic presentation of synthesis and purification method. After recycling a single peak is evident in HPLC, confirming the high purity of the material (Fig. S8b). Next, UV–Vis spectroscopy in dichloromethane (DCM) revealed the characteristic fingerprint of $(C_{59}N)_2$ that is in full agreement with the data reported in literature (Fig. S8c)[39].

[10]Cycloparaphenylene was synthesized following a modified strategy based on our recently published flow chemistry approach to CPPs[40]. Thereby, a 3 + 3 + 3 + 1 scheme combining was applied. The coupling of three 3-membered building blocks was done in batch, though, as well as the introduction of the last phenyl unit. The final aromatization was conducted analogous the published synthesis using sodium naphthalide, again, prepared in flow.

Scanning tunnelling microscopy

The scanning tunnelling microscopy (STM) measurements were performed with Aahrus type Specs microscope (model 150) at the CNR-IOM/Elettra joint laboratory for microscopy (OSMOS) in Trieste, Italy. The microscope is attached to an UHV preparation chamber equipped with evaporation cells and an Ar^+ ion sputter gun. The sample holding manipulator arm hosts a heating unit for thermal annealing with temperature control, and a quartz microbalance for evaporation rate monitoring.

Prior to each deposition of molecules, the Au surface was cleaned by at least two cycles of Ar^+ ion sputtering (1.5 keV) followed by thermal annealing to 720 K to obtain a clean and well-ordered (111) surface with sufficiently large terraces (~100 nm) that exhibits a distinct herring-bone reconstruction. After annealing, the surface was allowed to cool down and kept at RT during each deposition. The [10]CPP and $C_{59}N$ were vacuum deposited from laboratory made evaporating cells, each consisting of a boron nitride ceramic crucible with a tungsten filament wrapped around it and a K-type thermocouple for temperature control. To remove the impurities, the evaporation cells containing the [10]CPP and $(C_{59}N)_2$ powders were degassed for several hours before the first deposition. The typical evaporation temperature was 580 K for [10]CPP and in the range of 670 to 780 K for $C_{59}N$ with typical rate between 0.01 and 0.03 nm/min. The sample was transported to the STM device and analyzed immediately after each deposition.

All topographic images were acquired with the STM operating at RT and a chamber pressure in the range of 10^{-10} mbar. We used the STM in constant current mode (I = 100–800 pA) with a tungsten tip and negative sample bias. The lateral scale calibration of the images was performed a posteriori by taking the Au(111) surface lattice constants as a reference.

XPS, NEXAFS, and RPES spectroscopy

The XPS, NEXAFS, and RPES measurements were performed at the ALOISA beamline of the Elettra Synchrotron Facility, Trieste[41]. The Au(111) substrate surface was cleaned by repeated cycles of sputtering (1.5 kV Ar^+) and annealing up to 720 K. The $(C_{59}N)_2$ and [10]CPP were sublimed from laboratory made boron nitride crucibles, at a temperature of 670 K, up to 830 K, and at about 570 K, respectively. The chemical composition of the azafullerene layers was regularly checked during and after vacuum deposition by quantitative XPS of the $C_{59}N$/Au(111) and $C_{59}N$/[10]CPP/Au(111) layers. In these measurements we find no detectable O-containing impurities in XPS signals (Fig. S8d). Moreover, the XPS of the thick films from the same $C_{59}N$ batch present single N1*s* and C1*s* components with binding energies perfectly in line with previously reported values[19]. From the quantitative analysis of the C1*s* and N1*s* signals of $C_{59}N$ layers reported here we find the N:C = 1:60(±2) stochiometric ratio, which is in accordance with the studied azafullerene molecules and agrees with the previous studies of thick $C_{59}N$ layers. Therefore, within the precision and sensitivity of used surface spectroscopy techniques, no impurity (e.g., solvent) molecules could be detected in studied samples.

The overall film thickness of the deposited molecules have been determined from the intensity attenuation of the Au 4*f* peak due to inelastic scattering of photoelectrons passing through the organic overlayer[42]. Core level photoemission data were acquired in normal emission geometry with a constant 4° grazing angle of linearly p-polarized light beam with respect to the Au(111) surface plane. The C1*s* and N1*s* XPS spectra were acquired at a photon energy of 515 eV with a total energy resolution of 160 meV. Binding energies were calibrated with respect to the bulk spectral component of the Au $4f_{7/2}$ peak at 84.0 eV[43]. C K-edge and N K-edge NEXAFS spectra were acquired in partial electron yield mode by means of a channeltron multiplier equipped with a negatively biased grid (250 V and 370 V, respectively) to filter out low energy secondary electrons, in order to improve the signal to background ratio. NEXAFS spectra were acquired at two different orientations of the synchrotron beam with respect to the surface plane to probe the sample linear dichroism, namely transverse magnetic (TM, p-polarization) and transverse electric (TE, s-polarization) geometry, by sample rotation around the photon beam axis. The beam grazing angle was kept constant at 6°. The photon energy calibration and photon flux normalization methods are described in detail elsewhere[44]. Resonant photoemission was performed as a series of photoemission spectra across the nitrogen (carbon) K-edge with the photon energy tuned in steps of 0.1 eV through the N1*s* (C1*s*) absorption edge. The photon was incident at 4° and the photon polarization was set perpendicular to the surface (TM geometry, p-polarization). The electron analyzer was aligned with the sample normal and photon polarization. At each photon energy hv, single photoemission spectra were measured in a ~60 eV wide binding energy range up to the Fermi energy. All spectra have been merged in false color RPES intensity maps represented in kinetic energy (KE) scale in the form of $I(h\nu, \mathrm{KE})$. To highlight the resonant contribution in the

photoemission spectra, the non-resonant component (due to direct photoemission from molecular orbitals and from the substrate) has been measured at $h\nu = 395$ eV for the N1*s* and $h\nu = 280$ eV for the C1*s* RPES (below the resonant edge) and subtracted from all corresponding spectra. All measurements were carried out with the sample temperatures between 300 K and 430 K.

DFT calculations

For the NEXAFS spectra simulation first structure optimization DFT calculations were carried out using the ORCA code[45,46] with the B3LYP functional[47–50] and 6-31 G** basis set[51–56], and followed by vibrational frequency calculations. The default setting was used for the other parameters.

Next, hybrid time-dependent DFT (TD-DFT) calculations were performed with the B3LYP and ZORA-def2-TZVP[57–59] with def2/J auxiliary basis set. The spin-unrestricted TightSCF and RIJCOSX approximation were used and the other parameters were set to the default.

For the simulation of [10]CPP/Au(111), ground-state density functional calculations were carried out using the AIMPRO code[60–62] using the local density approximation for exchange-correlation energy[63]. Kohn–Sham wave functions for H, C, N and Au are constructed using localized Gaussian orbital functions multiplied by polynomials, with 18, 38, 40, and 40 independent functions, respectively ($l \leq 2$), with plane wave energy cut-off of 175 Ha. Calculations were spin optimized and polarized with different integer spin states tested (only the most stable are reported here). Relativistic pseudopotentials given by Hartwigsen, Goedecker, and Hutter (HGH)[64] with a finite electron Fermi temperature of $kT = 0.025$ eV were utilized. Systems were geometrically converged within a minimum of 10^{-6} a_B in position (here a_B is Bohr radius) and 10^{-6} Ha in energy.

To investigate orientation and electronic levels of the adsorbed CPP and CPP@C_{59}N structural optimization calculations were carried out allowing only the molecule to move and fixing the Au atoms of the slab. The molecules were first optimized in their isolated form in a 26 Å box. From a 3 atoms Au_{36} triple-layer Au(111) slab, we build and optimized a 6×6 supercell (108 atoms) in hexagonal supercells, allowing atoms and lattice parameter to vary with a $2 \times 2 \times 1$ k-point mesh, until reaching convergence ($a_O = 16.83$ Å). A cell *c*-axis spacing of >26 Å is chosen and fixed, to ensure there is no interaction between CPP and the base of the neighboring slab. The CPP spacing is essentially imposed by the choice of supercell and is close to experimental STM spacing. A single CPP was added in close-packed direction oriented along [1–10] on the unreconstructed Au(111) trilayer (16.83 Å CPP spacing, i.e., 1 CPP per 6×6 Au supercell). Once converged, the CPP distance from the slab and dihedral angle between phenyl neighbors were measured.

Data availability

The spectroscopic raw data and the essential beamline-specific normalization protocols to facilitate optimal reproducibility and interpretation of the presented spectra are available upon request to the corresponding authors.

References

1. Gaita-Ariño, A., Luis, F., Hill, S. & Coronado, E. Molecular spins for quantum computation. *Nat. Chem.* **11**, 301–309 (2019).
2. Köbke, A. et al. Reversible coordination-induced spin-state switching in complexes on metal surfaces. *Nat. Nanotechnol.* **15**, 18–21 (2020).
3. Morton, J. J. L. et al. High fidelity single qubit operations using pulsed electron paramagnetic resonance. *Phys. Rev. Lett.* **95**, 200501 (2005).
4. Morton, J. J. L. et al. Electron spin relaxation of N@C60 in CS2. *J. Chem. Phys.* **124**, 14508 (2006).
5. Morton, J. J. L. et al. Solid-state quantum memory using the 31P nuclear spin. *Nature* **455**, 1085–1088 (2008).
6. Pinto, D. et al. Readout and control of an endofullerene electronic spin. *Nat. Commun.* **11**, 6405 (2020).
7. Tanuma, Y. et al. Robust coherent spin centers from stable azafullerene radicals entrapped in cycloparaphenylene rings. *Nanoscale* **13**, 19946–19955 (2021).
8. Karan, S. et al. Spin manipulation by creation of single-molecule radical cations. *Phys. Rev. Lett.* **116**, 027201 (2016).
9. Terasaki, S. et al. Exfoliatable layered 2D honeycomb crystals of host-guest complexes networked by CH-π hydrogen bonds. *Angew. Chem. Int. Ed.* **63**, e202406502 (2024).
10. Yang, C. et al. Regulation of quantum spin conversions in a single molecular radical. *Nat. Nanotechnol.* https://doi.org/10.1038/s41565-024-01632-2 (2024).
11. Andreoni, W., Gygi, F. & Parrinello, M. Impurity states in doped fullerenes: C59B and C59. *N. Chem. Phys. Lett.* **190**, 159–162 (1992).
12. Hummelen, J. C., Knight, B., Pavlovich, J., González, R. & Wudl, F. Isolation of the Heterofullerene C 59N as its dimer (C 59N) 2. *Science* **269**, 1554–1556 (1995).
13. Butcher, F. H. et al. C59N monomers: stabilization through immobilization. *Phys. Rev. Lett.* **83**, 3478–3481 (1999).
14. Schulte, K., Wang, L., Moriarty, P. J., Prassides, K. & Tagmatarchis, N. Resonant processes and Coulomb interactions in (C59N)2. *J. Chem. Phys.* **126**, 184707 (2007).
15. Gruss, A., Dinse, K.-P., Hirsch, A., Nuber, B. & Reuther, U. Photolysis of (C 59N) 2 studied by time-resolved EPR. *J. Am. Chem. Soc.* **119**, 8728–8729 (1997).
16. Hasharoni, K., Bellavia-Lund, C., Keshavarz-K, M., Srdanov, G. & Wudl, F. Light-Induced ESR studies of the heterofullerene dimers. *J. Am. Chem. Soc.* **119**, 11128–11129 (1997).
17. Simon, F. et al. ESR signal in azafullerene (C 59N) 2 induced by thermal homolysis. *J. Phys. Chem. A* **103**, 6969–6971 (1999).
18. Stergiou, A. et al. A long-lived azafullerenyl radical stabilized by supramolecular shielding with a [10]cycloparaphenylene. *Angew. Chem. Int. Ed.* **58**, 17745–17750 (2019).
19. Tanuma, Y. et al. Noncontact layer stabilization of azafullerene radicals: route toward high-spin-density surfaces. *ACS Nano* **17**, 25301–25310 (2023).
20. Lewis, S. E. Cycloparaphenylenes and related nanohoops. *Chem. Soc. Rev.* **44**, 2221–2304 (2015).
21. Xia, J., Bacon, J. W. & Jasti, R. Gram-scale synthesis and crystal structures of [8]- and [10]CPP, and the solid-state structure of C60@[10]CPP. *Chem. Sci.* **3**, 3018 (2012).
22. Li, H. et al. Probing the deformation of [12]cycloparaphenylene molecular nanohoops adsorbed on metal surfaces by tip-enhanced Raman spectroscopy. *J. Chem. Phys.* **153**, 244201 (2020).
23. Zhang, J., Wang, C. & Taishan Wang, A. Fullerene in carbon nanoring: a saturn-like supramolecular complex. *Gen. Chem.* **7**, 200018–200018 (2021).
24. Wang, J., Cooper, G., Tulumello, D. & Hitchcock, A. P. Inner shell excitation spectroscopy of biphenyl and substituted biphenyls: probing ring–ring delocalization. *J. Phys. Chem. A* **109**, 10886–10896 (2005).
25. Stöhr, J. *NEXAFS Spectroscopy*, (Springer, 1992).
26. Deng, Y., Gao, B., Deng, M. & Luo, Y. A comparative theoretical study on core-hole excitation spectra of azafullerene and its derivatives. *J. Chem. Phys.* **140**, 0–11 (2014).
27. Schiller, F. et al. Electronic structure of C60 on Au(887). *J. Chem. Phys.* **125**, 144719 (2006).
28. Zhao, C. et al. Supramolecular complexes of C80-based metallofullerenes with [12]cycloparaphenylene nanoring and altered property in a confined space. *J. Phys. Chem. C* **123**, 12514–12520 (2019).

29. Dresselhaus, M. S., Dresselhaus, G. & Eklund, P. C. Electronic Structure. in *Science of Fullerenes and Carbon Nanotubes* 1st edn, 413–463 (Elsevier, 1996).
30. Brühwiler, P. A., Karis, O. & Mårtensson, N. Charge-transfer dynamics studied using resonant core spectroscopies. *Rev. Mod. Phys.* **74**, 703–740 (2002).
31. Menzel, D. Ultrafast charge transfer at surfaces accessed by core electron spectroscopies. *Chem. Soc. Rev.* **37**, 2212–2223 (2008).
32. Coville, M. & Thomas, T. D. Molecular effects on inner-shell lifetimes: possible test of the one-center model of Auger decay. *Phys. Rev. A* **43**, 6053–6056 (1991).
33. Föhlisch, A. et al. Direct observation of electron dynamics in the attosecond domain. *Nature* **436**, 373–376 (2005).
34. Kladnik, G. et al. Ultrafast charge transfer through noncovalent Au–N interactions in molecular systems. *J. Phys. Chem. C* **117**, 16477–16482 (2013).
35. Kladnik, G. et al. Ultrafast charge transfer pathways through a prototype amino-carboxylic molecular junction. *Nano Lett.* **16**, 1955–1959 (2016).
36. Batra, A. et al. Quantifying through-space charge transfer dynamics in π-coupled molecular systems. *Nat. Commun.* **3**, 1086 (2012).
37. Schiros, T. et al. Donor-acceptor shape matching drives performance in photovoltaics. *Adv. Energy Mater.* **3**, 894–902 (2013).
38. Ueno, H., Nishihara, T., Segawa, Y. & Itami, K. Cycloparaphenylene-based ionic donor–acceptor supramolecule: Isolation and characterization of Li+ @C 60 ⊂[10]CPP. *Angew. Chem. Int. Ed.* **54**, 3707–3711 (2015).
39. Hummelen, J. C., Prato, M. & Wudl, F. There is a hole in my bucky. *J. Am. Chem. Soc.* **117**, 7003–7004 (1995).
40. Griwatz, J. H., Kessler, M. L. & Wegner, H. A. Continuous-flow synthesis of cycloparaphenylene building blocks on a large scale. *Chem. Eur. J.* **29**, e202302173 (2023).
41. Floreano, L. et al. Performance of the grating-crystal monochromator of the ALOISA beamline at the Elettra synchrotron. *Rev. Sci. Instrum.* **70**, 3855–3864 (1999).
42. Cumpson, P. J. & Seah, M. P. Elastic scattering corrections in AES and XPS. II. Estimating attenuation lengths and conditions required for their valid use in overlayer/substrate experiments. *Surf. Interface Anal.* **25**, 430–446 (1997).
43. Cossaro, A., Floreano, L., Verdini, A., Casalis, L. & Morgante, A. Comment on 'local methylthiolate adsorption geometry on Au(111) from photoemission core-level shifts''. *Phys. Rev. Lett.* **103**, 119601 (2009).
44. Floreano, L. et al. Periodic arrays of Cu-phthalocyanine chains on Au(110). *J. Phys. Chem. C* **112**, 10794–10802 (2008).
45. Neese, F. The ORCA program system. *WIREs Comput. Mol. Sci.* **2**, 73–78 (2012).
46. Neese, F. Software update: The ORCA program system—version 5.0. *WIREs Comput. Mol. Sci.* **12**, e1606 (2022).
47. Becke, A. D. Density-functional thermochemistry. III. The role of exact exchange. *J. Chem. Phys.* **98**, 5648–5652 (1993).
48. Lee, C., Yang, W. & Parr, R. G. Development of the Colle–Salvetti correlation-energy formula into a functional of the electron density. *Phys. Rev. B* **37**, 785–789 (1988).
49. Vosko, S. H., Wilk, L. & Nusair, M. Accurate spin-dependent electron liquid correlation energies for local spin density calculations: a critical analysis. *Can. J. Phys.* **58**, 1200–1211 (1980).
50. Stephens, P. J., Devlin, F. J., Chabalowski, C. F. & Frisch, M. J. Ab initio calculation of vibrational absorption and circular dichroism spectra using density functional force fields. *J. Phys. Chem.* **98**, 11623–11627 (1994).
51. Clark, T., Chandrasekhar, J., Spitznagel, G. W. & Schleyer, P. V. R. Efficient diffuse function-augmented basis sets for anion calculations. III. The 3-21+G basis set for first-row elements, Li–F. *J. Comput. Chem.* **4**, 294–301 (1983).
52. Hariharan, P. C. & Pople, J. A. The influence of polarization functions on molecular orbital hydrogenation energies. *Theor. Chim. Acta* **28**, 213–222 (1973).
53. Hehre, W. J., Ditchfield, R. & Pople, J. A. Self—consistent molecular orbital methods. XII. Further extensions of Gaussian—type basis sets for use in molecular orbital studies of organic molecules. *J. Chem. Phys.* **56**, 2257–2261 (1972).
54. Pritchard, B. P., Altarawy, D., Didier, B., Gibson, T. D. & Windus, T. L. New basis set exchange: an open, up-to-date resource for the molecular sciences community. *J. Chem. Inf. Model.* **59**, 4814–4820 (2019).
55. Feller, D. The role of databases in support of computational chemistry calculations. *J. Comput. Chem.* **17**, 1571–1586 (1996).
56. Schuchardt, K. L. et al. Basis set exchange: a community database for computational sciences. *J. Chem. Inf. Model.* **47**, 1045–1052 (2007).
57. Weigend, F. & Ahlrichs, R. Balanced basis sets of split valence, triple zeta valence and quadruple zeta valence quality for H to Rn: design and assessment of accuracy. *Phys. Chem. Chem. Phys.* **7**, 3297 (2005).
58. Lenthe, E., van, Baerends, E. J. & Snijders, J. G. Relativistic regular two-component Hamiltonians. *J. Chem. Phys* **99**, 4597–4610 (1993).
59. van Wüllen, C. Molecular density functional calculations in the regular relativistic approximation: method, application to coinage metal diatomics, hydrides, fluorides and chlorides, and comparison with first-order relativistic calculations. *J. Chem. Phys.* **109**, 392–399 (1998).
60. Briddon, P. R. & Jones, R. LDA calculations using a basis of Gaussian orbitals. *Phys. Status Solidi.* **217**, 131–171 (2000).
61. Rayson, M. J. Rapid filtration algorithm to construct a minimal basis on the fly from a primitive Gaussian basis. *Comput. Phys. Commun.* **181**, 1051–1056 (2010).
62. Briddon, P. R. & Rayson, M. J. Accurate Kohn–Sham DFT with the speed of tight binding: current techniques and future directions in materials modelling. *Phys. Status Solidi.* **248**, 1309–1318 (2011).
63. Grimme, S. Semiempirical GGA-type density functional constructed with a long-range dispersion correction. *J. Comput. Chem.* **27**, 1787–1799 (2006).
64. Hartwigsen, C., Goedecker, S. & Hutter, J. Relativistic separable dual-space Gaussian pseudopotentials from H to Rn. *Phys. Rev. B* **58**, 3641–3662 (1998).

Acknowledgements

The authors acknowledge financial support by the Japanese JSPS Overseas Research Fellowship scheme (Y.T.), the Slovenian Research Agency (research projects J1-3007 (D.A. and G.K.), J2-2514 (G.K.), N1-0220 (D.A.) and research programs P1-0112 (D.C. and G.K.), P1-0125 (D.A.), P1-0099 (M.v.M.M.), the EUR LUMOMAT project and the Investments for the Future ANR-18-EURE-0012 (C.E. and B.A.), the PHC Proteus Agreement 46151XJ (C.E., B.A., and D.A.) and the Ministries of Europe and Foreign Affairs (MEAE) and Higher Education and Research (MESR), the COST Action CA21126 (C.E., Y.T., and D.A.). Part of this study was carried out within the National Quantum Science and Technology Institute (NQSTI) and received funding from the European Union Next-Generation EU (PIANO NAZIONALE DI RIPRESA E RESILIENZA (PNRR)— MISSIONE 4 COMPONENTE 2, INVESTIMENTO 1.3—PE_00000023 (A.M.)). L.F., A.G., and G.B. acknowledge partial funding from the European Union's Horizon 2020 research and innovation program under grant agreement No 101007417, having benefited from the access provided by CNR-IOM in Trieste within the framework of the NFFA-Europe Pilot Transnational Access Activity, proposal [ID447]. DFT calculations were performed at the CCIPL (Centre de Calcul Intensif des Pays de la Loire) (C.E. and B.A.). NEXAFS simulation calculations were carried out at the HPC facilities of Faculty of Mathematics and Physics, University of Ljubljana, Slovenia.

Author contributions

D.C., G.K., and D.A. conceived and designed this work. L.S., D.C., G.K., G.B., L.F., and A.M. performed NEXAFS, XPS and RPES experiments, D.C. and G.K. analyzed the data. L.S., G.B., L.F., and A.G. performed the RT STM experiments, and M.v.M.M., E.Z., and G.K. performed the LT STM; Y.T., B.A., and C.P.E. performed DFT calculations; I.K.S., N.T., J.V., and H.A.W. synthesized and characterized $C_{59}N$ and [10]CPP. All authors contributed to the analysis and interpretation of the results and editing of the manuscript.

Competing interests

The authors declare no competing interests.

Additional information

Supplementary information The online version contains supplementary material available at https://doi.org/10.1038/s41467-024-55521-2.

Correspondence and requests for materials should be addressed to Denis Arčon or Dean Cvetko.

Peer review information *Nature Communications* thanks the anonymous reviewers for their contribution to the peer review of this work. A peer review file is available.